Int. J. Heat Mass Transfer. Vol. 36, No. 10, pp. 2589–2599, 1993
Printed in Great Britain

0017-9310/93 $6.00+0.00

Effects of momentum ratio on turbulent nonreacting and reacting flows in a ducted rocket combustor

T. M. LIOU, L. CHEN and Y. Y. WU
National Tsing Hua University, Hsinchu, Taiwan 300, R.O.C.

(*Received* 31 *August* 1992 *and in final form* 9 *November* 1992)

Abstract—A numerical study of turbulent nonreacting and reacting flows in a ducted rocket combustor with an ASM turbulence model and a finite-rate combustion model is reported. In addition, detailed measurements of flow velocities and turbulence parameters have been conducted by use of a four-beam two-color LDV system. Three different values of the ratio of fuel momentum to air momentum were selected to investigate its effects on the turbulent flow structure, mixing and combustion characteristics. It is found that the momentum ratio has strong effects on the number, size and rotational direction of dome region recirculation zones, reattachment length, axial fuel-jet spreading rate and penetration ability, flame temperature distributions and total pressure loss in the ducted rocket combustor. A useful correlation between the reattachment length and momentum ratio is derived. Moreover, a moderate value of the momentum ratio is recommended for better combustion performance and lower total pressure loss. The reported data are believed to provide valuable guidelines for practical design of combustors.

1. INTRODUCTION

SIDE-DUMP combustors have been widely used in high-technology aerospace applications with severe volume constraints. The flow field of a side-dump combustor is very complex, involving flow recirculation, jet impingement, flow separation and reattachment, turbulent mixing of fuel and air, chemical reactions, etc. All these phenomena are affected by a host of geometric and aerodynamic parameters such as dome height, side-inlet flow angle, fuel injector configuration and fuel-to-air momentum ratio. The size of the recirculation region is crucial to the performance of a side-dump combustor because it serves to enhance the flow-mixing and anchor the flame. An efficient combustion chamber requires complete mixing and combustion of the fuel with air within a minimum combustor length and pressure loss [1]. The penetration and mixing characteristics of an axial jet crossly injected into two opposing side jets have important engineering applications, particularly pertaining to the design in gas turbine combustors and ramjet combustors. For gas turbine combustors, the most important independent flow variable was found to be the momentum ratio [2]. Therefore, there is a need to study the effects of the momentum ratio on the turbulent flow mixing in a side-dump combustor.

Although a systematic numerical analysis of the effects of combustor parameters on the mixing and combustion performance of the side-dump combustors has been conducted by several research groups [3–7], the reports of jet momentum ratio effects on the turbulent flow-mixing in the side-dump combustors are scarce. Experimental investigations of the side-dump combustor flows have been conducted by numerous workers [8–11], but their works were restricted to the effects of combustor geometries. Only Hsieh *et al.* [12] and Schadow and Chieze [13] were interested in the effects of the momentum ratio on the turbulent flow-mixing. The former performed a flow measurement in a simulated ducted rocket combustor which is one variant of the side-dump combustors, by using Laser–Doppler Velocimetry (LDV) to obtain the flow pattern and jet interactions as a function of the ram-air momentum and the fuel-rich jet momentum. The latter conducted water tunnel and windowed combustion tests to gain a qualitative insight into the effects of the momentum ratio on the turbulent flow mixing. Schadow and Chieze claimed that a proper fuel-to-air momentum ratio should be adopted to achieve high combustion efficiency and that two basic requirements must be satisfied: (1) in the dome region a near-stoichiometric gaseous fuel/air mixture ratio should be established, and gas-phase combustion should be initiated in this region; (2) the reacting plume should penetrate into the airstream to achieve good mixing. The aforementioned works have provided useful information on the ducted rocket combustor. However, only the flowfield data or the qualitative trends between flow-mixing and combustion efficiency are reported. No work provides direct comparisons between the experimental and theoretical results. The purpose of the present study is to fill some of these voids. Three different values of fuel-to-air

Address correspondence to: Professor Tong-Miin Liou, Department of Power Mechanical Engineering, National Tsing Hua University, Hsinchu, Taiwan 30043, R.O.C.

NOMENCLATURE

C	mean scalar property
c	fluctuating part of C
$C_k, C_\varepsilon, C_1, C_2$	empirical constants in the turbulence model
$C_{A1}, C_{A2}, C_{\theta 1}, C_{\theta 2}$	empirical constants in ASM model
C_{pt}	coefficient of total pressure loss
f	mixture fraction
H	total enthalpy; height of combustor
h	static enthalpy; height of axial jet
h_f^0	heat of formation
J	fuel-to-air jet momentum ratio, M_a/M_s
k	turbulent kinetic energy
L_d	dome height
M_a	momentum of axial fuel jet
M_s	momentum of side air jets
p	mean static pressure
P_{ic}	production rate of $\overline{u_i c}$
P_{ij}	production rate of $\overline{u_i u_j}$
P_k	production rate of k
Re	Reynolds number, $\rho U_{ref} H/\mu$
s	stoichiometric ratio
S_c	source term; mean chemical reaction rate
U	axial mean velocity
u	axial fluctuating velocity
u'	root mean square of u
U_i	mean velocity in the X_i-direction
U_{ref}	combustor bulk mean velocity, 23.9 m s^{-1}
V	transverse mean velocity
v	transverse fluctuating velocity
v'	root mean square of v
w	side jets width
X	combustor axial coordinate
X^*	normalized combustor axial coordinate, $X \geqslant 0$, $X^* = X/H$; $X \leqslant 0$, $X^* = X/L_d$
X_r^*	nondimensional reattachment length
X_i	spatial coordinate in the i-direction
Y	combustor transverse coordinate
Y^*	normalized combustor transverse coordinate, $Y/(H/2)$
Y_i	mass fraction for ith species
z_p	distance normal to the wall.

Greek symbols

γ	mass diffusivity
δ_{ij}	Kronecker delta
ε	dissipation rate of k
ε_{ij}	dissipation rate of $\overline{u_i u_j}$
μ	molecular viscosity
μ_t	turbulent viscosity
ρ	fluid density
$\sigma_k, \sigma_\varepsilon$	turbulent Prandtl number of k and ε, respectively
ϕ_{ij}	pressure redistribution of $\overline{u_i u_j}$
ϕ_{ic}	pressure redistribution of $\overline{u_i c}$.

Subscripts

a	value at air inlet
f	value at fuel inlet
fu	fuel
i	ith species.

momentum ratio were selected to obtain, both numerically and experimentally, a quantitative insight into the effects of the momentum ratio on the flow structure and turbulent flow mixing.

The k–ε model of turbulence is considered to be the best among the two-equation models. For flows with significant streamline curvature, adverse pressure gradient and high shear, a k–ε model is inadequate and it is necessary to go to higher order turbulence models. The Reynolds stress model (designated as RSM) is marginally better than the algebraic stress model (designated as ASM). However, the model sophistication and additional computer cost make the RSM model less attractive for application to combustor flow calculations. The ASM model appears attractive for accounting the effects of the streamline curvature and anisotropy in an economical fashion. Consequently, the ASM model is adopted in the present work.

For reacting flow, the mathematical difficulty arises in calculations of mean chemical reaction rate due to incorporating turbulent fluctuations in temperature and species concentrations. To circumvent this difficulty, several combustion models have been proposed. The simplest combustion model for the diffusion flame is to use a single-step fast-chemistry assumption whereby the reaction goes to completion as soon as the fuel and oxidizer are mixed. The need to evaluate the mean reaction rate is thereby removed. For turbulent diffusion flames, the fuel and oxidizer may exist at the same location but at different times; therefore, it is necessary to take account of the fluctuations in mixture fraction. The most popular approach of achieving this phenomenon is using an assumed form of the probability density function in terms of the mean and variance of f [14]. Even though the fast-chemistry combustion model provides a quantitative description of temperature and flow patterns for many practical combustors, this model leads to serious errors in the computed flame temperature. A finite-rate reaction must be considered if more information is required. A multistep, finite rate combustion model provides a more accurate prediction. However, it increases complexity and computer time for combustor calculations. In this study, a single-step finite-rate combustion model based on Arrhenius and eddy break-up concepts is adopted for an alternative approach.

Detailed measurements of side-dump combustor flow fields were made using LDV in the present work, since the flow reversal in the dome region and the large turbulence fluctuations generated by the jet-to-jet impingement make the use of the hot-wire technique impractical. Furthermore, the above literature survey reveals that turbulence information is still lacking, and this fact has encouraged the authors to characterize the flowfield in terms of mean velocity, turbulence intensity, and Reynolds stress components.

2. THEORETICAL FORMULATION

2.1. *Governing equations*

The conservation equations of mass, momentum and conserved scalar for the two-dimensional steady incompressible flow can be expressed in tensor notation as follows

$$\frac{\partial}{\partial X_i}(\rho U_i) = 0 \tag{1}$$

$$\frac{\partial}{\partial X_j}(\rho U_j U_i) = -\frac{\partial P}{\partial X_i} + \frac{\partial}{\partial X_j}\left[\mu\left(\frac{\partial U_i}{\partial X_j}+\frac{\partial U_j}{\partial X_i}\right)-\rho\overline{u_i u_j}\right] \tag{2}$$

$$\frac{\partial}{\partial X_i}(\rho U_i C) = \frac{\partial}{\partial X_i}\left[\rho\gamma\left(\frac{\partial C}{\partial X_i}\right)-\rho\overline{u_i c}\right]+S_c. \tag{3}$$

The combustion is treated as a single-step, irreversible, finite-rate reaction. Therefore, equation (3) represents three equations: the mixture fraction f, total enthalpy H, and the fuel mass fraction Y_{fu}. The mixture fraction f is defined as

$$f = \frac{\xi-\xi_a}{\xi_f-\xi_a} \tag{4}$$

where the variable ξ represents any conserved property free from sources and sinks. If the adiabatic wall is assumed, the total enthalpy can be obtained by

$$H = H_a + f(H_f - H_a) \tag{5}$$

where

$$H = \sum Y_i h_i + 0.5(U^2+V^2). \tag{6}$$

Since the specific heat C_{p_i} of individual species is a function of temperature, the static enthalpy h_i is given as

$$h_i = \int_{T_0}^{T_f} C_{p_i}(T)\,\mathrm{d}T + h_{fi}^0. \tag{7}$$

The specific heat C_{p_i} and the static enthalpy h_i are obtained as a function of temperature from JANAF tables [15].

The mixture fraction has a zero S_c, whereas the fuel mass fraction Y_{fu} has a non-zero S_c. Equations (2) and (3) are not closed because of the presence of the terms $\rho\overline{u_i u_j}$, $\rho\overline{u_i c}$, and S_c. In the following, the turbulence closures are first examined and then a discussion of the combustion models for S_c is presented.

2.2. *Turbulence model*

In the Reynolds stress model the following transport equations of Reynolds stresses and Reynolds scalar fluxes are solved.

$$\frac{\partial}{\partial X_k}(U_k\overline{u_i u_j}) = D_{ij}+P_{ij}+\phi_{ij}-\varepsilon_{ij} \tag{8}$$

$$\frac{\partial}{\partial X_k}(U_k\overline{u_i c}) = D_{ic}+P_{ic}+\phi_{ic}-\varepsilon_{ic} \tag{9}$$

where the terms on the right-hand side of equations (8) and (9) are the diffusion, production, pressure redistribution and viscous dissipation of $\overline{u_i u_j}$ and $\overline{u_i c}$, respectively. To reduce the computational efforts, Rodi's approximation [16] is adopted. Equations (8) and (9) under Rodi's assumption that the transport of $\overline{u_i u_j}$ and $\overline{u_i c}$ are proportional to the transport of k with the multiplication factor $\overline{u_i u_j}/k$ and $\overline{u_i c}/2k$ [17], respectively, can be simplified to algebraic forms in terms of k, ε, and derivatives of mean flow and scalar fields.

$$\frac{\overline{u_i u_j}}{k}(P_k-\varepsilon) = P_{ij}+\phi_{ij}-\varepsilon_{ij} \tag{10}$$

$$\frac{\overline{u_i c}}{2k}(P_k-\varepsilon) = P_{ic}+\phi_{ic}-\varepsilon_{ic} \tag{11}$$

where the exact terms P_{ij}, P_{ic} and P_k can be written as

$$P_{ij} = -\overline{u_i u_k}\frac{\partial U_j}{\partial X_k}-\overline{u_j u_k}\frac{\partial U_i}{\partial X_k} \tag{12}$$

$$P_{ic} = -\overline{u_k c}\frac{\partial U_i}{\partial X_k}-\overline{u_i u_k}\frac{\partial C}{\partial X_k} \tag{13}$$

$$P_k = \tfrac{1}{2}P_{ii}. \tag{14}$$

The pressure redistribution term ϕ_{ij} acts to redistribute energy among the various components and to reduce the shear stresses. It can be modeled as the sum of three contributions,

$$\phi_{ij} = \phi_{ij,1}+\phi_{ij,2}+\phi_{ij,w} \tag{15}$$

where Rotta's linear return to isotropic model has been adopted for $\phi_{ij,1}$ and the isotropization production model is used for $\phi_{ij,2}$ [18].

$$\phi_{ij,1} = -C_{A1}\frac{\varepsilon}{k}(\overline{u_i u_j}-\tfrac{2}{3}\delta_{ij}k) \tag{16}$$

$$\phi_{ij,2} = -C_{A2}(P_{ij}-\tfrac{2}{3}\delta_{ij}P_k). \tag{17}$$

The wall-proximity effect on ϕ_{ij} is expressed as in ref. [19]

$$\phi_{ij,w} = \left[0.125\frac{\varepsilon}{k}(\overline{u_i u_j} - \tfrac{2}{3}\delta_{ij}k) + 0.015(P_{ij} - Q_{ij})\right]\frac{k^{3/2}}{\varepsilon z_p} \quad (18)$$

where

$$Q_{ij} = -\overline{u_i u_k}\frac{\partial U_k}{\partial X_j} - \overline{u_j u_k}\frac{\partial U_k}{\partial X_i}. \quad (19)$$

The dissipation rate ε_{ij} is modeled by assuming that the flow is locally isotropic.

$$\varepsilon_{ij} = \tfrac{2}{3}\delta_{ij}\varepsilon. \quad (20)$$

Similarly, ϕ_{ic} is the counterpart of ϕ_{ij} and can be modeled as follows [20]

$$\phi_{ic} = -C_{\theta 1}\frac{\varepsilon}{k}\overline{u_i c} + C_{\theta 2}\overline{u_k c}\frac{\partial U_i}{\partial X_k} + \phi_{ic,w} \quad (21)$$

$$\phi_{ic,w} = 0.25\frac{\varepsilon}{k}\overline{u_i c}\,\delta_{ip}\frac{k^{3/2}}{\varepsilon z_p} \quad (22)$$

$$\varepsilon_{ic} = 0. \quad (23)$$

In order to complete the ASM model, the transport equations for k and ε are also needed.

$$\frac{\partial}{\partial X_i}(\rho U_i k) = \frac{\partial}{\partial X_i}\left[C_k\left(\rho\frac{k}{\varepsilon}\overline{u_i u_j}\right)\frac{\partial k}{\partial X_i}\right] - \rho\overline{u_i u_j}\frac{\partial U_i}{\partial X_j} - \rho\varepsilon \quad (24)$$

$$\frac{\partial}{\partial X_i}(\rho U_i \varepsilon) = \frac{\partial}{\partial X_i}\left[C_\varepsilon\left(\rho\frac{k}{\varepsilon}\overline{u_i u_j}\right)\frac{\partial \varepsilon}{\partial X_i}\right] - C_1\frac{\varepsilon}{k}\rho\overline{u_i u_j}\frac{\partial U_i}{\partial X_j} - C_2\rho\frac{\varepsilon^2}{k}. \quad (25)$$

For the present study, the model constants are shown as follows as suggested by Gibson and Launder [21]:

$$C_{A1} = 1.8;\quad C_{A2} = 0.6;\quad C_{\theta 1} = 3.0;$$
$$C_{\theta 2} = 0.5;\quad C_k = 0.22;\quad C_\varepsilon = 0.15;$$
$$C_1 = 1.44 \quad \text{and} \quad C_2 = 1.92.$$

2.3. *Combustion model*

The mean reaction rate S_c in equation (3) must be determined to complete the formulation. In this work, methane is used to simulate the fuel-rich exhausted gases, a single-step finite-rate reaction is employed, and the stoichiometric combustion equation on a molar basis is

$$CH_4 + 2(O_2 + nN_2) \rightarrow CO_2 + 2H_2O + 2nN_2. \quad (26)$$

The mean source term for fuel is calculated from standard kinetic rate expressions using local temperature and species concentrations. Since the combustion processes in an SDR combustor are mixing-controlled under most conditions, the turbulent fluctuations can significantly alter the reaction rates; therefore, an eddy break-up model [22] is incorporated into the combustion model to account for the turbulence–chemistry interaction. The mean source term for fuel is thus given by

$$S_{fu} = -\text{MIN}\,[R_{EBU}, A\rho^a Y_{fu}^b Y_{O_2}^c \exp(-E/RT)] \quad (27)$$

and

$$R_{EBU} = 4\rho\frac{\varepsilon}{k}\text{MIN}\left[Y_{fu}, \frac{Y_{O_2}}{s}\right] \quad (28)$$

where the chemical kinetic parameters are $A = 6.7\times 10^{12}$, $E = 48.4$ kcal mol^{-1}, $a = 1.5$, $b = 0.2$ and $c = 1.3$ according to Westbrook and Dryer [23]. When the values of unburnt fuel mass fraction Y_{fu} and the mixture fraction f are known, the mass fractions of other species can be determined by the following relations [24]:

$$Y_{O_2} = (1-f)Y_{O_2,a} - \frac{2W_{O_2}}{W_{fu}}(fY_{fu,f} - Y_{fu}) \quad (29a)$$

$$Y_{CO_2} = \frac{W_{CO_2}}{W_{fu}}(fY_{fu,f} - Y_{fu}) \quad (29b)$$

$$Y_{H_2O} = \frac{2W_{H_2O}}{W_{fu}}(fY_{fu,f} - Y_{fu}) \quad (29c)$$

$$Y_{N_2} = 1 - Y_{fu} - Y_{O_2} - Y_{CO_2} - Y_{H_2O}. \quad (29d)$$

Once the species mass fractions are known, the fluid properties, such as mean temperature and mixture density, can be determined by equation (7) and the perfect gas law.

2.4. *Boundary conditions*

(1) Symmetric axis ($Y = 0$)

$$\frac{\partial U}{\partial Y} = \frac{\partial C}{\partial Y} = \frac{\partial k}{\partial Y} = \frac{\partial \varepsilon}{\partial Y} = 0, \quad V = 0$$

where

$$C = f,\quad Y_{fu} \quad \text{(only for reacting flow)}.$$

(2) Axial-inlet

$$U = \text{measured } U_{in},\quad V = \text{measured } V_{in}$$
$$k = \text{measured } k_{in},\quad \varepsilon_{in} = C_\mu k_{in}^{3/2}/(0.03h)$$
$$C_\mu = 0.09$$
$$f = 1.$$

For reacting flow

$$H_f = \sum Y_{i,f}\left[\int_{T_0}^{T_f} C_{p_i}(T)\,dT + h_{fi}^0\right] + 0.5U^2$$
$$Y_{fu,f} = 0.2,\quad Y_{N_2,f} = 0.8$$
$$T_f = 1000\ \text{K}$$

$P_f = 517$ kPa.

(3) Side-inlets

$U =$ measured U_{in}, $V =$ measured V_{in}

$k =$ measured k_{in}, $\varepsilon_{in} = C_\mu k_{in}^{3/2}/(0.03w)$

$f = 0.$

For reacting flow

$$H_a = \sum Y_{i,a}\left[\int_{T_0}^{T_a} C_{p_i}(T)\,\mathrm{d}T + h_{fi,a}^0\right] + 0.5V^2$$

$Y_{O_2,a} = 0.232$, $Y_{N_2,a} = 0.768$

$T_a = 500$ K

$P_a = 517$ kPa.

(4) Outlet ($X^* = 9$)

$$\frac{\partial U}{\partial X} = \frac{\partial C}{\partial X} = \frac{\partial k}{\partial X} = \frac{\partial \varepsilon}{\partial X} = 0, \quad V = 0.$$

(5) Walls

In the near-wall region the wall-function treatment is employed to link no-slip wall to the fully turbulent region [25]. A non-catalytic wall is assumed for species mass fraction. The values of the Reynolds stresses and Reynolds fluxes are stored at scalar grid points and evaluated by using the algebraic relations; therefore, boundary conditions are not required.

3. SOLUTION PROCEDURE

The governing equations and boundary conditions are solved numerically by using the power law finite differencing and staggered, non-uniform grids. The SIMPLE algorithm of Patankar and Spalding [26] is used here to solve these equations. When the ASM model is employed, the Reynolds stresses appear explicitly in the momentum equation; this equation is source-term dominated and therefore leads to the coefficient matrix lacking of diagonal dominance. In order to improve the numerical stability, Iacovides and Launder [27] proposed four stability-promoting measures in predicting turbulent momentum and heat transfer in coils and U-bends. In this study two measures are adopted to enhance the solution convergence:

(1) $\frac{\partial}{\partial X_i}\left[\left(\mu+\frac{\mu_t}{\sigma_k}\right)\frac{\partial k}{\partial X_i}\right]$ and $\frac{\partial}{\partial X_i}\left[\left(\mu+\frac{\mu_t}{\sigma_\varepsilon}\right)\frac{\partial \varepsilon}{\partial X}\right]$ are used to replace the diffusion terms in equations (24) and (25), and the solution convergence is found to be more computationally stable [28];

(2) the Reynolds stress is divided into an apparent viscosity multiplying a mean strain (i.e. Boussinesq type) part and a residual stress part; the residual stress part is treated in the computer program as a source term.

A double loop iteration scheme is used to obtain convergent solutions to the equations. The mean flow velocity, mixture fraction, fuel mass fraction, and turbulence model variables (k and ε) are solved in an outer loop using the Gauss–Seidel line-by-line iteration with under-relaxation factor from 0.4 to 0.6. For each outer-loop iteration, the Reynolds stresses and Reynolds fluxes are computed from equations (6) and (7) in an inner loop using the Gauss–Seidel point iteration with under-relaxation factor of 0.3.

Grid independence testing is conducted by comparing the solutions for one flow case on grid sizes of 35×20, 53×29 and 70×40. The results of this comparison indicates that the 35×20 is not grid independent and that the 53×29 grid solution is essentially identical to 70×40 grid solution. Consequently, the 53×29 grid size, which is finer than that of refs. [3] and [5], is chosen in the present work. The iterative sequence was terminated when the overall sums of the non-dimensionalized mass residual fell below 5×10^{-4}.

4. EXPERIMENTAL SET-UP

4.1. *Experimental system*

A schematic drawing of the overall experimental system is plotted in Fig. 1. Air was drawn into the test chamber through settling chambers, honeycombs and screens, bellmouth contractions (10:1), and side-inlets by a 10 hp turbo blower at the downstream end. The axial jet was provided through a 152:1 contraction by a 5 hp blower located upstream of the axial inlet. The air in the chamber then flowed through a rectangular duct, a flow straightener, a rotameter, a bellows, and was exhausted by the turbo blower. The velocity measurements were taken with a two-color four-beam component LDV system. A 5 W argon-ion laser provided the coherent light source. The 514.5 nm (green) and 488 nm (blue) lines were first separated into four beams. Each of the two pairs of beams had one beam Bragg-shifted by 40 MHz to eliminate the ambiguity of flow direction and fringe bias. The two pairs of beams were finally focused into the test model to form a probe volume consisting of two nominally orthogonal sets of fringes. The optical system was aligned so that the two sets of fringes in the probe volume were inclined at 46.1 and $-43.9°$ to the combustor centerline for measurements of $U+V$ and $U-V$ components of velocity. The probe volume can be positioned with 0.01 mm resolution by mounting the focusing lens on a three-axis traversing table.

The seeding particles were introduced into the air stream by twelve atomizers symmetrically located on the walls of the three settling chambers. The atomizers were operated by filtered compressed air and salt water and produced particles in the size range of 0.5–5 μm. The salt solution was mixed to give a nominal 0.8 μm particle after the droplet dried. The detected signals were electrically downmixed to the appropriate frequency shift of 2–10 MHz in the present work.

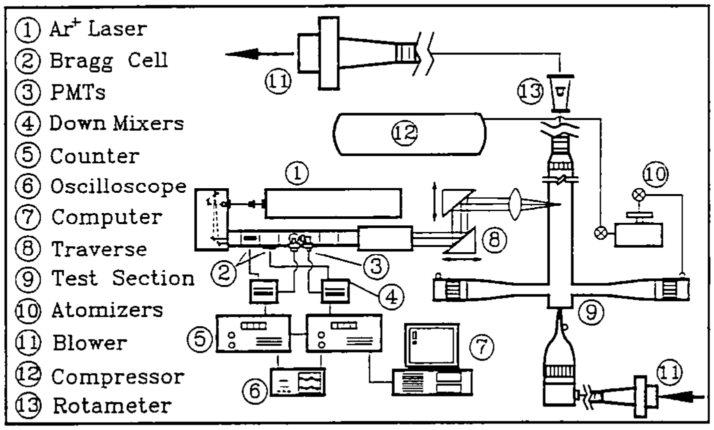

FIG. 1. Schematic drawing of overall experimental system.

Then two counter processors with 1 ns resolution were used to process the Doppler signals. The Doppler signals were monitored on an oscilloscope and the digital outputs of the counter processors were fed directly to a microcomputer for storage and analysis.

4.2. *Test model and conditions*

The two-dimensional test model consisted of two short rectangular side-inlet ducts, an axial injection slit, and a rectangular chamber. The two 20 mm long rectangular side-inlet ducts intersected the chamber walls at an angle of 90° and were separated aximuthally by 180°, whereas the injection slit was located at the center of the head plate and directed along the chamber axis (Fig. 1). The internal dimensions of the side-inlet ducts and the axial injection slit were 15×120 and 1.6×120 mm^2, respectively. The chamber model was made of 5 mm thick Plexiglas and the chamber duct had a cross-sectional area of 30×120 mm^2 and was 2015 mm long from the head plate to the exit.

The measurements were made along the central plane $Z = 0$. A two-dimensionality check of the spanwise axial and transverse mean velocity profiles was performed. The measured profiles highly supported the two-dimensionality (within 2.7% U_{ref}). A chamber bulk mean velociity of 23.9 m s^{-1} was used as a reference to nondimensionalize the experimental results. The Reynolds number based on the combustor height and bulk mean velocity was 4.56×10^4. A single Reynolds number was adopted in the present work since the mean flow field was approximately invariant for $2.9 \times 10^3 < Re < 2.0 \times 10^5$, as found for the case without an axial jet [7]. Moreover, the head plate was fixed at one-half combustor height upstream from $X^* = 0$ (Fig. 2) according to the fact that at this position the fraction of the inlet mass flow rate bifurcated into the dome region is maximum [7].

5. RESULTS AND DISCUSSION

5.1. *Nonreacting flow*

5.1.1. *Mean flow pattern.* Figure 3 shows the contours of streamline for three different values of momentum ratio. The streamlines are expressed by using the normalized stream function. Figure 3(a) depicts the flow pattern in the front portion of the ducted rocket combustor for $J = 1.28$, where J is defined as the momentum ratio of axial fuel to the side air. Only a single clockwise vortex is generated in the dome region, similar to those found in the side-dump combustor without an axial jet [7]. For $J = 0.11$ and $J = 0.025$ (Figs. 3(b), (c)) the flow structures have similar patterns, but they are different in size and strength. There are two counter-rotating vortices in the

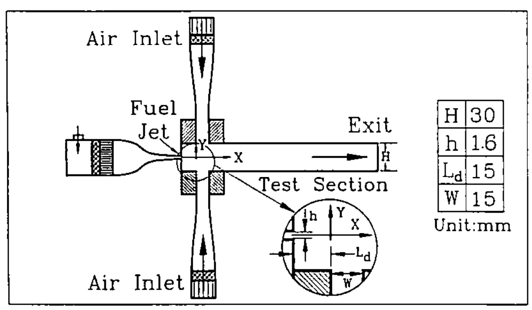

FIG. 2. Sketch of configuration, coordinate system, and dimensions of combustor model.

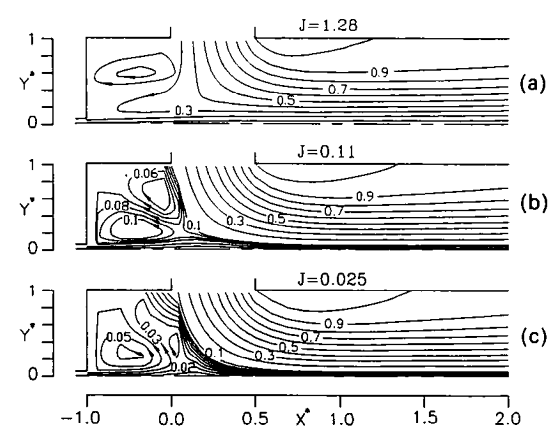

FIG. 3. Predicted mean-flow streamlines: (a) $J = 1.28$; (b) $J = 0.11$; (c) $J = 0.025$.

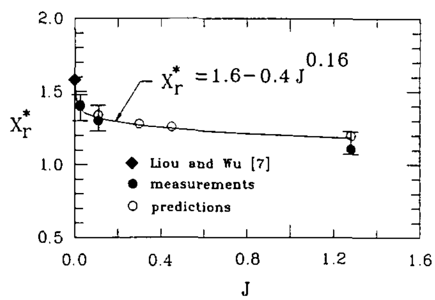

FIG. 4. Effects of momentum ratio on reattachment length.

dome region, a larger one located near the axial jet with a counter-clockwise direction and a smaller one located near the side inlet jet with clockwise direction. It can be seen that the flow pattern in Fig. 3(a) is quite different from those in Figs. 3(b) and (c).

Each part of Fig. 3 also shows a separation bubble located immediately downstream of the side inlet port due to the sharp turning of the side jet. Experimentally, the mean reattachment point was first located by use of flow visualization with a light thread and then further determined by near-wall LDV scanning around (1 mm from the wall) the visual reattachment point. Since the reattachment length is a sensitive parameter that has been used to assess the overall predictive capability of turbulence models [29], a comparison between the predictions and measurements is shown in Fig. 4 and the agreement is reasonably good. Moreover, both the computational and experimental results indicate a decrease of reattachment length with increasing momentum ratio. The reattachment length vs momentum ratio can be further correlated by a simple relation $X_r^* = 1.6\text{–}0.4\,J^{0.16}$, which has not been reported previously in the literature. Also note that X_r^* approaches 1.6 as J approaches zero, that is very close to 1.58 reported by Liou *et al.* [7].

5.1.2. *Concentration profiles and turbulent mixing.* Since there are no available concentration data, only numerical results are reported. The calculated fuel and air concentration profiles for cold flow are presented in Fig. 5; these plots reveal significant influence of the momentum ratio on the fuel and air concentration profiles, especially in the dome region ($-1 < X^* < 0$) and jet impinging zone ($0 < X^* < 0.5$). For $J = 1.28$ (Fig. 5(a)), in connection with streamline pattern (Fig. 3(a)), the axial fuel jet is so strong that it can penetrate through the side-inlet jets and acts as a horizontal plate, resulting in a large amount of side-jet air bifurcating into the dome region. There is virtually no fuel deflected into the dome region by the side air jet. Consequently, the clockwise rotating vortex in the dome region, as shown in Fig. 3(a), makes very little contribution to promoting the turbulent mixing of fuel and air. The spreading of the axial jet half-width (dashed line in Fig. 5) for $J = 1.28$ is therefore narrow in the dome region and similar to that of a two-dimensional plane jet. For $J = 0.11$ (Fig. 5(b)), the axial fuel jet partly penetrates through and is partly deflected by the side air jets, thereby some fraction of the axial-inlet fuel turns back into the dome region and a portion of side-inlet air is entrained by the recirculating axial jet (Fig. 3(b)) in the dome region. Hence, the axial jet of $J = 0.11$ is expected to spread faster than that of $J = 1.28$, as shown in Fig. 5. For $J = 0.025$ (Fig. 5(c)) the penetration of axial jet is poor, since the side air jets act like a vertical wall which causes the axial fuel jet to be almost completely

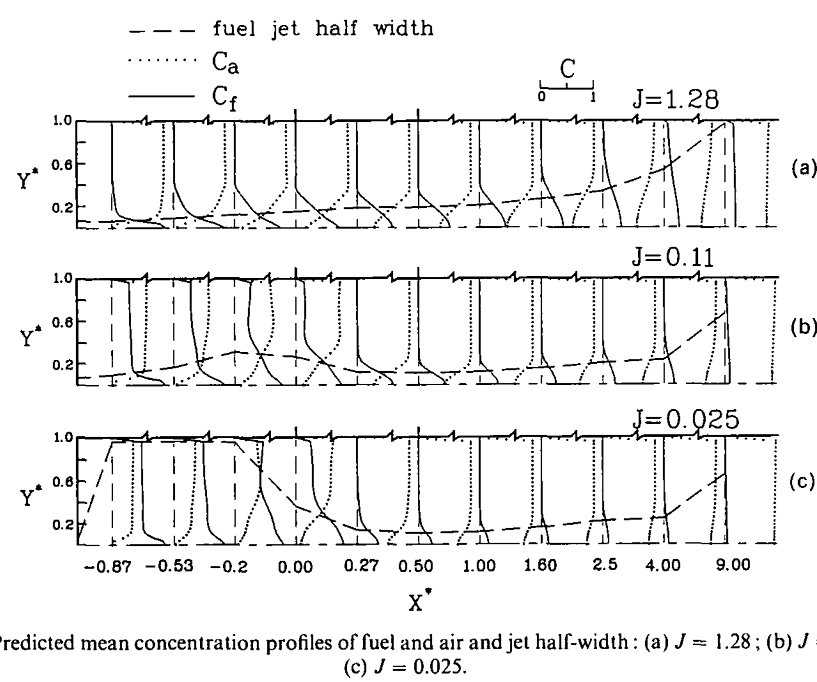

FIG. 5. Predicted mean concentration profiles of fuel and air and jet half-width: (a) $J = 1.28$; (b) $J = 0.11$; (c) $J = 0.025$.

deflected, resulting in a larger amount of fuel trapped in the dome region and a smaller portion of air entrained by the large recirculating fuel stream. Therefore, the jet half-width of $J = 0.025$ grows abruptly in the dome region. The above phenomena account for why the air concentration is prevailing in the dome region for $J = 1.28$, whereas the fuel concentration is prevailing in the dome region for $J = 0.025$.

5.1.3. *Mean velocity and turbulence parameters.* The axial mean velocity profiles acquired by LDV measurements and ASM model predictions are shown in Fig. 6. The velocity gradients are steep in the dome region and gradually attenuated as the flow moves downstream. The flow is unidirectional as $X^* \geqslant 4$ and becomes nearly fully developed as $X^* = 9$. The comparisons between the predicted and measured axial mean velocity profiles at various axial stations show that the agreement is fairly good.

Selected results of the measured and predicted turbulence intensities u', v', and Reynolds stress $-\overline{uv}$ for $J = 1.28$ are plotted in Fig. 7. It shows that the maximum turbulence intensities and shear stresses occur around the central axis where gradients of the mean velocity are steep, as shown in Fig. 6(a). Because of space restrictions the data of $J = 0.11$ and $J = 0.025$ are not shown here. Downstream of the side-inlet jets additional peaks of u', v' and $-\overline{uv}$ are generated due to the formation of shear layers of the separation bubble. As the flow proceeds downstream of the reattachment point, the maximum values of u', v' and $-\overline{uv}$ shift away from the combustor axis. In both the impingement and the fully developed regions, agreement between computations and measurements

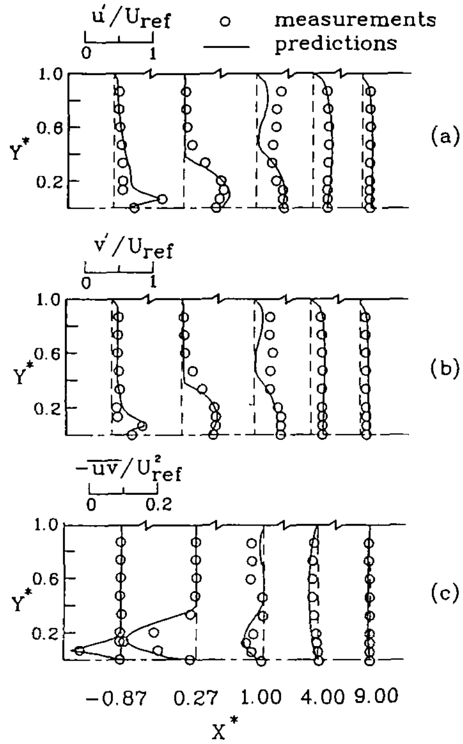

FIG. 7. Predicted and measured profiles of: (a) axial turbulence intensity; (b) transverse turbulence intensity; (c) Reynolds stress, for $J = 1.28$.

are reasonably good. The turbulent parameters are under-predicted in the regions of separation bubbles and over-predicted around the central axis in the dome region where high shear flows are generated by the axial inlet.

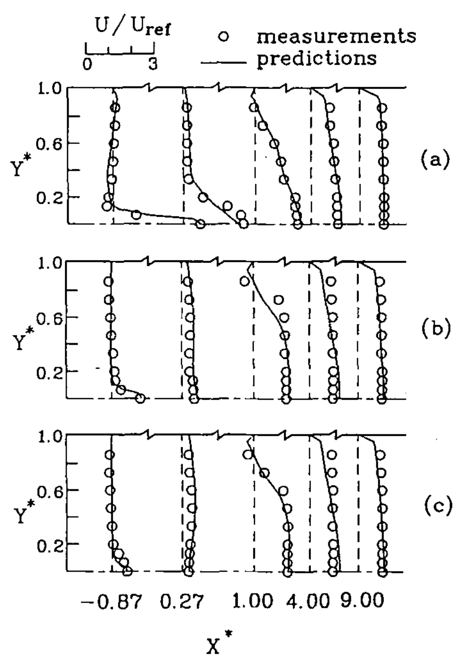

FIG. 6. Predicted and measured profiles of mean axial velocity: (a) $J = 1.28$; (b) $J = 0.11$; (c) $J = 0.025$.

5.2. *Reacting flow*

The profiles of the major mass fractions of reactants and products and temperature at two selected X^* stations are shown in Figs. 8 and 9, respectively. As noted before, the axial fuel jet of $J = 0.11$ spreads faster than that of $J = 1.28$; therefore, there exists a more intense combustion between the axial-inlet fuel and side-inlet air in the dome region for $J = 0.11$. This fact accounts for why the transverse temperature and mass fraction distributions of $J = 0.11$, Fig. 8(b), are more uniform and their levels are averagely higher than those of $J = 1.28$, Fig. 8(a), in the dome region. For $J = 0.025$, the axial jet half-width grows abruptly in the dome region as addressed in Section 5.1.2, and thus the temperature and mass fraction distributions are rather uniform; however, since a smaller fraction of air is entrained into the dome region and reacted with fuel, the temperature and product mass fraction levels of $J = 0.025$ (shown in Fig. 8(c)) are lower than those of $J = 0.11$. At $X^* = -0.5$, no residual oxygen is found in $J = 0.11$ and $J = 0.025$. A comparison of the centerline Y_{CH_4} at $X^* = -0.5$ with that at $X^* = 0.5$ indicates a decrease of the centerline Y_{CH_4}

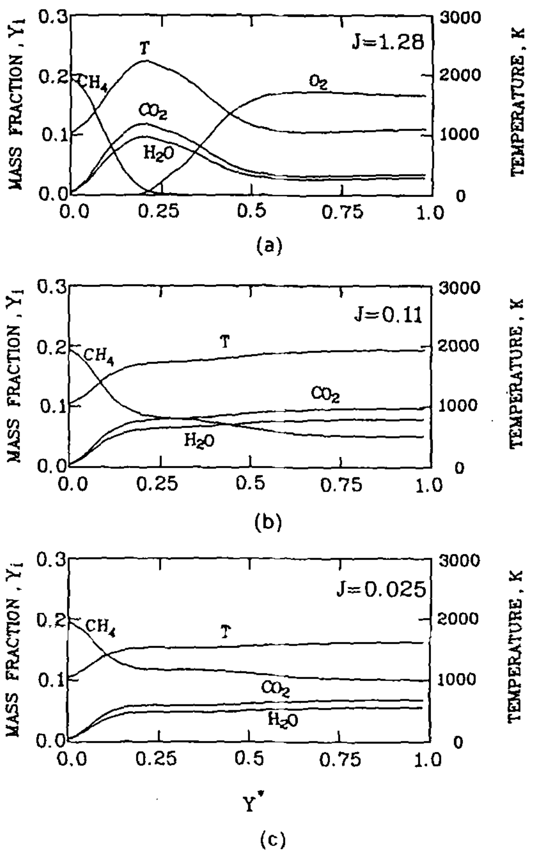

FIG. 8. Predicted profiles of mass fractions and temperature at $X^* = -0.5$: (a) $J = 1.28$; (b) $J = 0.11$; (c) $J = 0.025$.

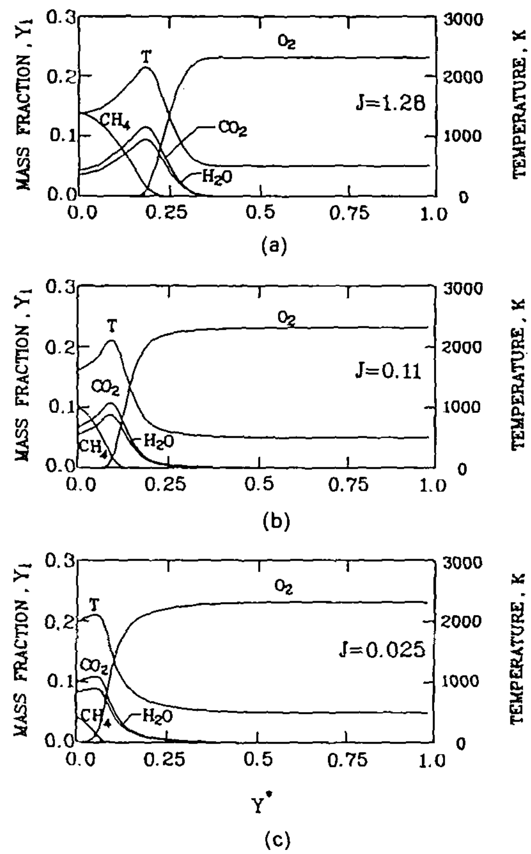

FIG. 9. Predicted profiles of mass fractions and temperature at $X^* = 0.5$: (a) $J = 1.28$; (b) $J = 0.11$; (c) $J = 0.025$.

with increasing X^* as a result of the fuel consumption. At $X^* = 0.5$, there is a small overlap region between Y_{CH_4} and Y_{O_2}, in which a significant chemical reaction takes place. Note that the smooth temperature variation near the peak temperature zones is due to the finite-rate chemical reaction. In fact, Fig. 9 depicts that at $X^* = 0.5$ the intense combustion is confined in the region of $0 < Y^* < 0.25$ for all three cases studied and shifts towards the combustor centerline with decreasing momentum ratio. Since the axial position X^*, where the intense combustion occurs on the combustor centerline, may be used to define the flame length, Fig. 9 suggests that the flame length decreases with decreasing momentum ratio.

Figure 10 shows the contour maps of the isotherm pattern of reacting flow. The high temperature zones are represented by the dashed lines. Since the axial fuel jet of $J = 1.28$ spreads so slowly in the dome region (Fig. 5(a)), the fuel/air combustion occurs mainly at the boundary of the fuel jet. In contrast, from the data presented earlier it is known that better fuel/air mixing in the dome region is achieved for $J = 0.11$ and 0.025. The combustion in the dome region for $J = 0.11$ and 0.025 is thus not limited along the fuel jet boundary and the temperature distribution in the dome region is more uniform. Figure 10 further shows that the temperature distribution is most uniform and the temperature level is highest in the dome region for $J = 0.11$ among the three momentum ratios investigated. The intersection of the peak temperature zones with the combustor axis, as shown in Fig. 10, also provides the information of flame length which is in agreement with the observation made from Fig. 9, that is, the flame length decreases with decreasing momentum ratio. From the above discussion it can be concluded that among the three cases studied, only the $J = 0.11$ case has a moderate flame length and approximately satisfies the two critical requirements addressed in ref. [13], as mentioned in the Introduction. By comparing Fig. 3 with Fig. 10, it can be seen that the turbulent flow combustion characteristics are closely correlated with the cold flow streamline patterns and, hence, the momentum ratios.

Figure 11 shows the effect of combustion on the mean axial velocity pattern for $J = 1.28$. The dense axial mean-velocity contours for the reacting flow case indicate the burnt gas expansion and acceleration resulting from heat release of combustion. In the presence of combustion, the dome recirculation zone is slightly narrower and the reattachment length is about 46% shorter than that of the cold flow case. Previous experiments of reacting flows in a co-axial dump combustor [30] also demonstrated a 44% decrease of the

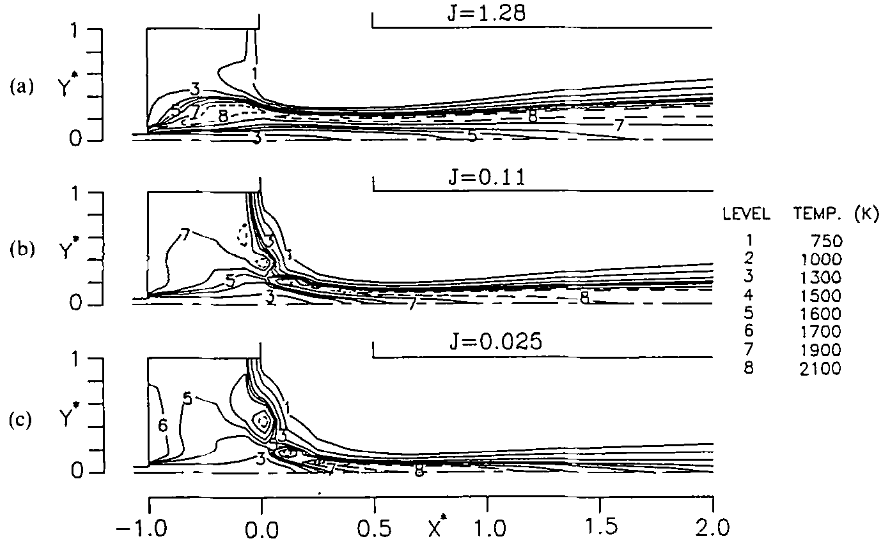

FIG. 10. Predicted isotherm contours for: (a) $J = 1.28$; (b) $J = 0.11$; (c) $J = 0.025$.

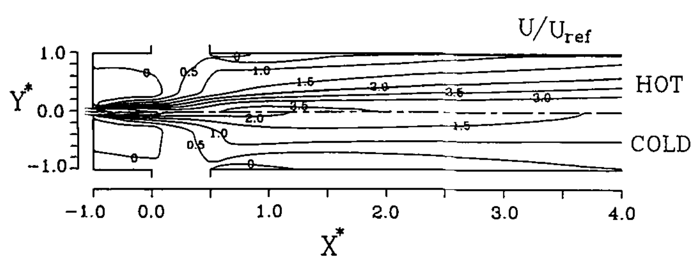

FIG. 11. The effect of combustion on the mean axial velocity pattern for $J = 1.28$.

reattachment length from the corresponding cold flow case.

5.3. *Centerline total-pressure distributions*

The centerline pressure of cold flow is measured by use of the Pitot tube. The distributions of total pressure loss coefficient C_{pt} of cold and hot flow are shown in Fig. 12. It is found that a higher fuel jet momentum leads to a higher total pressure loss. For the cold flow case, the numerical predictions show quite good agreement with the experimental data. Figure 12,

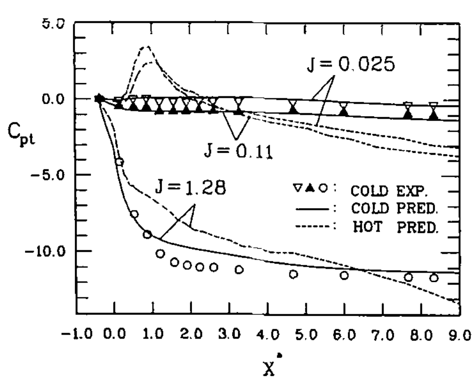

FIG. 12. Effect of momentum ratio on total pressure loss.

together with Figs. 3 and 10, again suggests that the $J = 0.11$ case is better than the other two cases.

5. SUMMARY AND CONCLUSIONS

The quantitative effects of the ratio of fuel momentum to air momentum on flowfield structure, and the mixing and combustion characteristics have been studied both computationally and experimentally by correlating the mean streamline patterns, reattachment lengths, mass fraction and temperature profiles, isotherm contours, mean velocity profiles, turbulent intensities, Reynolds stresses and total pressure loss coefficients. Based on these results the following conclusions can be drawn:

(1) the number, size and rotational direction of the recirculation zones in the dome region depend strongly on the ratio of fuel momentum to air momentum;

(2) the reattachment length increases with decreasing momentum ratio. A simple correlation of $X_r^* = 1.6 - 0.4J^{0.16}$ is obtained for the first time;

(3) as the momentum ratio increases, both the axial-jet penetration ability and the total pressure loss increase; however, the spreading rate of axial fuel jet decreases; and

(4) the moderate momentum ratio, $J \simeq 0.11$, is

preferable to the other two momentum ratios for the reason of a better combination of turbulent mixing and combustion in the dome region, flame length, and overall pressure loss.

A detailed comparison of single-step infinite-rate, single-step finite-rate, and multistep finite-rate combustion models is being undertaken and will be submitted for publication in the near future.

Acknowledgement—This research was partly supported by the National Science Council of the Republic of China under contract No. NSC-80-0401-E007-02.

REFERENCES

1. L. T. Chittilapilly, S. Venkateswaran, P. J. Paul and H. S. Mukunda, Flow measurements in a model ramjet secondary combustion chamber, *J. Propulsion Power* **6**, 727–731 (1990).
2. K. S. Chen and J. Y. Hwang, Experimental study on the mixing of one- and dual-line heated jets with a cold crossflow in a confined channel, *AIAA J.* **29**, 353–360 (1991).
3. L. Chen and C. C. Tao, Study of the side-inlet dump combustor of solid-ducted rocket with reacting flow, *AIAA* Paper 84-1378 (1984).
4. S. P. Vanka, R. R. Craig and F. D. Stull, Mixing, chemical reaction, and flowfield development in ducted rockets, *J. Propulsion Power* **2**, 331–338 (1986).
5. D. L. Cherng, V. Yang and K. K. Kuo, Theoretical study of turbulent reacting flows in a solid-propellant ducted rocket combustor, *J. Propulsion Power* **5**, 678–685 (1989).
6. D. L. Cherng, V. Yang and K. K. Kuo, Simulations of three-dimensional turbulent reacting flows in solid-propellant ducted rocket combustors, *AIAA* Paper 88-3042 (1988).
7. T. M. Liou, S. M. Wu and Y. H. Hwang, Experimental and theoretical investigation of turbulent flow in a side-inlet rectangular combustor, *J. Propulsion Power* **6**, 131–138 (1990).
8. P. R. Choudhury, Characteristics of a side dump gas generator ramjet, *AIAA* Paper 82-1258 (1982).
9. T. M. Liou and S. M. Wu, Flowfield in a dual inlet side-dump combustor, *J. Propulsion Power* **4**, 53–60 (1988).
10. K. A. Zetterstrom, B. Sjoblom and A. Jarnmo, Solid ducted rocket engine combustor tests, *6th Int. Symp. Air Breathing Engines* 9–16 (1983).
11. J. A. Schetz and B. D. Thompson, Water flow tests of a ducted rocket combustor, *AIAA* paper 85-1107 (1985).
12. W. H. Hsieh, C. L. Chuang, A. S. Yang, D. L. Cherng, V. Yang and K. K. Kuo, Measurement of flowfield in a simulated solid-propellant ducted rocket combustor using laser doppler velocimetry, *AIAA* paper 89-2789 (1989).
13. K. C. Schadow and D. J. Chieze, Water tunnel and windowed combustion as tools for ducted rocket development, *JANNAF Propulsion Meeting* CPIA-PUB-400, 101–115 (1981).
14. K. K. Kuo, *Principles of Combustion*, Chap. 7. John Wiley & Sons, New York (1986).
15. D. R. Stull and H. Prophet, JANAF thermochemical tables (2nd Edn), NSRDS—Report 37, National Bureau of Standards (1971).
16. W. Rodi, A new algebraic relation for calculating the Reynolds stresses, *ZAMM* **56**, T219–T221 (1976).
17. M. S. Hossain and W. Rodi, A turbulence model for buoyant flows and its application to vertical buoyant jets. In *Turbulent Buoyant Jets and Plumes* (Edited by W. Rodi), pp. 121–146. Pergamon Press, Oxford (1982).
18. B. E. Launder, On the effects of a gravitational field on the turbulent transport of heat and momentum, *J. Fluid Mech.* **67**, 569–581 (1975).
19. B. E. Launder, G. J. Reece and W. Rodi, Progress in the development of a Reynolds-stress turbulent closure, *J. Fluid Mech.* **68**, 537–566 (1975).
20. B. E. Launder and D. S. A. Samaraweera, Application of a second-moment tubulence closure to heat and mass transport in thin shear flows—I. Two-dimensional transport, *Int. J. Heat Mass Transfer* **22**, 1631–1641 (1979).
21. M. M. Gibson and B. E. Launder, Ground effects on pressure fluctuation in the atmospheric boundary layer, *J. Fluid Mech.* **86**, 491–511 (1978).
22. B. F. Magmussen and B. H. Hjertager, On mathematical modeling of turbulent combustion with special emphasis on soot formation and combusion, *16th Int. Symp. Combustion* 719–729 (1978).
23. C. K. Westbrook and F. L. Dryer, Simplified reaction mechanism for the oxidation of hydrocarbon fuels in flames, *Combustion Sci. Tech.* **27**, 31–43 (1981).
24. F. A. Williams, *Combustion Theory: the Fundamental Theory of Chemically Reacting Flow Systems* (2nd Edn), pp. 74–75. Benjamin-Cummings, Menlo Park, California (1985).
25. B. E. Launder and D. B. Spalding, The numerical computation of turbulent flows, *Computer Meths Appl. Mech. Engng* **3**, 269–289 (1974).
26. S. V. Patankar and D. B. Spalding, A calculation procedure for heat, mass and momentum transfer in three-dimensional parabolic flows, *Int. J. Heat Mass Transfer* **15**, 1787–1806 (1972).
27. H. Iacovides and B. E. Launder, ASM predictions of turbulent momentum and heat transfer in coils and U-bends, *Proc. 4th Int. Conf. Numerical Methods in Laminar and Turbulent Flow*, Swansea, 1023–1045 (1985).
28. B. K. Sultanian, Numerical modeling of turbulent swirling flow downstream of an abrupt pipe expansion, Ph.D. Thesis. Arizona State University, Tempe (1984).
29. D. M. Driver and H. L. Seegmiller, Features of a reattaching turbulent shear layer in divergent channel flow, *AIAA J.* **23**, 163–171 (1985).
30. S. A. Ahmed and A. S. Nejad, Premixed, turbulent combustion of axisymmetric sudden expansion flows, *Int. J. Heat Fluid Flow* **13**, 15–21 (1992).